

The Shapley Supercluster. II. Spectroscopic observations in a wide area and general morphology

H. Quintana¹, Eleazar R. Carrasco², and Andreas Reisenegger¹

Received _____; accepted _____

The Astronomical Journal, in press

¹Departamento de Astronomía y Astrofísica, Pontificia Universidad Católica de Chile, Casilla 306, Santiago 22, Chile.

²Instituto Astronômico e Geofísico, Universidade de São Paulo, Caixa Postal 3386, 01060-970, São Paulo, Brazil.

ABSTRACT

We report 2868 new multi-object spectroscopic measurements of galaxy redshifts in an area roughly $12^\circ \times 6^\circ$ (right ascension \times declination) centered on the Shapley Supercluster (SSC). These correspond to 2627 different galaxies. Including other measurements reported in the literature, the total number of galaxies with measured redshifts in a $19^\circ \times 16^\circ$ area centered on the supercluster now reaches 5090. Of these, 2949 lie in the redshift range 9,000 - 18,000 km s^{-1} , which we tentatively identify with the SSC. This unprecedented sample allows a quite detailed qualitative morphological study of the SSC. Based on the three-dimensional distribution of galaxies and clusters of galaxies, we identify several sub-condensations of the supercluster, as well as walls and filaments connecting them. We also find another supercluster in the background, at redshift $\sim 23,000$ km s^{-1} .

Subject headings: catalogs — surveys — galaxies: clusters: general — galaxies: distances and redshifts — cosmology: observations — large-scale structure

1. Introduction

Shapley (1930) was the first to note a “remote cloud of galaxies” with a “great linear dimension, ... numerous population, and distinctly elongated form” at $\alpha = 13^h 30^m$, $\delta = -30^\circ$ in the direction of Centaurus and Hydra. This cloud, commonly known today as the Shapley Supercluster (hereafter SSC), is located at a distance of $\sim 140h^{-1}$ Mpc (taking the Hubble constant as $H_0 = 100h$ km s^{-1} Mpc^{-1}), beyond the Hydra-Centaurus supercluster (at $\sim 40h^{-1}$ Mpc). The SSC appears to be the most massive concentration of matter at $z < 0.1$ (Scaramella et al. 1991; Raychaudhuri 1989, 1991; Zucca et al. 1993; Einasto et al.

1997; but see also Batuski et al. 1999 for evidence for other, comparable structures). Over the last 20 years, several efforts have been underway to collect data at different wavelength bands, in order to map the matter distribution and evaluate the dynamical state of the SSC. A first effort in this direction was the work of Melnick & Quintana (1981), as a part of a program to study the physical properties of x-ray clusters. This study was extended to cover a significant fraction of the clusters in the area to estimate the masses of the member clusters and trace the mass distribution in the supercluster, as first discussed by Melnick & Moles (1987) using data reported by Quintana et al. (1995). The central region (around the clusters A 3558, A 3556, and A 3562) and other major clusters have also been studied optically by Cristiani et al. (1987), Metcalfe et al. (1987), Teague et al. (1990), and recently by Bardelli and collaborators (Bardelli et al. 1994, 1998, 2000). Several papers have investigated the X-ray emission of clusters in the general area (Raychaudhury et al. 1991; Breen et al. 1994; Ettori et al. 1997) and particularly in the core region of the SSC (Kull & Böhringer 1999; Hanami et al. 1999)

The SSC is a high-density region comprising more than 30 Abell clusters of galaxies (Abell et al. 1989, hereafter referred to as ACO) within a radius of $\sim 25h^{-1}$ Mpc. The central core is dominated by ACO clusters A 3556, A 3558, and A 3562 and two poor clusters. Two other main concentrations are present, formed by ACO clusters A 3528/3530/3532 and A 3570/3571/3572/3575.

This is Paper II in a series on spectroscopic observations of the Shapley supercluster region initiated by Quintana et al. (1995; hereafter Paper I). Paper I discussed spectroscopic observations in the central region of the SSC, and used them to estimate its mass and its effect on the motion of the Local Group. Here, we present a significantly extended sample, including further radial velocities of galaxies observed on a wide area which extends approximately from $12^h 53^m$ to $13^h 46^m:5$ in right ascension and -28° to -34° in declination,

and thus covers $11.5^\circ \times 6^\circ$, or $\sim 26 \times 14h^{-2}$ Mpc² at the mean redshift of the SSC ($z \sim 0.05$). These data are combined with redshifts from the literature, covering (more sparsely and irregularly) the area $12^h 40^m$ to $14^h 10^m$ in right ascension and -23° to -39° in declination ($19^\circ \times 16^\circ$ or $45 \times 37h^{-2}$ Mpc²) to give a total sample of 5090 galaxy redshifts. These are used for a qualitative study of the general shape of the distribution of galaxies in the SSC, which includes filaments and sheets. In Paper III (Reisenegger et al. 2000) we discuss the global supercluster dynamics and show that the central region is bound and currently collapsing. This has implications for the spatial interpretation of the structure in the central regions of the SSC, which we discuss below. We leave for Paper IV (Carrasco et al. 2000) the discussion of the dynamics and other properties of the individual clusters of galaxies.

2. Observations

The spectroscopic observations were carried out using the fiber spectrograph mounted on the 2.5 m (100") DuPont telescope at Las Campanas Observatory (LCO), in several observing sessions. The weather conditions in all sessions were good, with relatively good seeing and dark sky. The multifiber system consists of a plug plate at the focal plane, with 128 fibers running to a spectrograph coupled to the 2D-Frutti detector (Shethman 1989). 105 to 112 fibers were used for objects. Sixteen sky fibers were set aside, spaced at intervals of one every 6 fibers along the spectrograph entrance, and positioned in a random pattern in the plug plate. Standard quartz lamp exposures of a white spot inside the dome were used to correct for pixel-to-pixel variations of the detector. The grating angle was changed to several values during these long exposures in order to properly illuminate the whole detector surface. Five-minute exposures with helium-neon and thorium-argon hollow-cathode comparison lamps were taken for wavelength calibration before and after

each exposure. The resulting 2D-Frutti images have a 2048×1520 pixel area. The fiber images are ~ 8 pixels wide, separated by ~ 12 pixels from center to center. Thirty-four fields of $1.5^\circ \times 1.5^\circ$ were observed in seven sessions, covering a combined area of $11.5^\circ \times 6^\circ$. The exposure times were adjusted between 60 and 180 minutes, depending on the brightness of the galaxies and the available observing time. Table 1 gives a schedule of our seven observing sessions. A total of 2868 galaxy spectra were obtained, corresponding to 2627 different galaxies whose two-dimensional distribution is shown in Figure 1. The observations were made with some overlap, except for fields 383-G and 383-H.

The positions of the observed galaxies were taken from the Digitized Sky Survey (DSS). The galaxy selection was carried out on the DSS images displayed on a computer screen, giving priority to elliptical and bright galaxies, but avoiding what appeared to be obvious foreground objects. For each fiber field a total of 120 candidate target galaxies were chosen by eye. The fiber assignment program discarded close objects (within $30''$ of each other) or galaxies that fell on fiber holes from other fields that were drilled on the same metallic plug plate. The low priority assigned to spiral or irregular-looking objects and the lack of an objective photometric catalog imply that extreme care must be exercised for any statistically oriented analysis of our velocity sample. It does not have a well-defined magnitude cut-off and has a strong bias in morphological selection.

Gaps and areas remaining to complete a full rectangular area down to $\delta = -35.5^\circ$ have been observed later. The full data set will be published once the reduction of these remaining data is complete.

3. Reductions

All reductions were performed inside the IRAF¹ environment. Velocity determinations were carried out using the cross-correlation technique and identifying and fitting line profiles by eye. A complete discussion of the reduction process is given in Quintana et al. (1996). Here we give a summary of the reductions. The fiber+2D-Frutti system presents an S-shaped distortion of the spectra, inherent to this instrument. A sixth-order cubic spline was fitted to trace this shape. The IRAF Hydra package was used to extract spectra from the two-dimensional array, correct pixel-to-pixel variations via dome flats, use a fiber transmission table for appropriate sky subtraction, and put the spectra on a linear wavelength scale. The eighteen sky spectra from each exposure were combined via a median filter and subtracted from each of the object spectra. The final sky-subtracted spectra are based on the relative flux normalization of the 5577Å, 5890Å, and 6300Å night-sky lines. The wavelength solutions for 20-30 points using a 4th or 5th-order Chebyshev polynomial typically yielded rms residual values $< 0.5 \text{ \AA}$. With a 600 line mm^{-1} grating blazed at 5000Å, the final galaxy spectra have a resolution of $\sim 10\text{\AA}$, a pixel scale of $\sim 2.6\text{\AA}$ and a wavelength range of $\sim 3500 - 6900\text{\AA}$.

The radial velocities of the galaxies were determined by two different methods. For non-early-type spectra (i.e. emission lines, E+A, etc.), a line-by-line Gaussian fit was used and the resulting velocities from each line fit were averaged. For normal early-type spectra, the XCSAO cross-correlation algorithm in the IRAF RVSAO package (Kurtz et al. 1992) was used (this algorithm is described in Tonry & Davis 1979). Four template spectra with a high signal-to-noise ratio were used to correlate with the observed spectra in order to determine the radial velocities of the galaxies. Two of the *templates* used here were galaxy

¹IRAF is distributed by NOAO, which is operated by the Association of Universities for Research in Astronomy Inc., under contract with the National Science Foundation.

spectra taken with the fiber instrument (NGC 1407 and NGC 1426). Another template, galaxy NGC 1700, was from the previous detector (Spectograph) mounted on the same telescope, and one was synthetic. The synthetic template was constructed from the stellar spectra library of Jacoby et al. (1984), using the ratios of stellar light for the E0 galaxy NGC 1374 from the synthesis studies of Pickles (1985). The R value (see Tonry & Davis 1979 for details) was used as a reliability factor of the quality of the measured velocity. For $R > 4$, the template which gave the lowest error value, out of the four radial velocity cross-correlation templates mentioned above, is used as resulting velocity. (This method gave more consistent results than other combinations we tried, such as a mean of the results of the four correlations.) For $R \leq 4$, we looked at the spectra and tried line-by-line Gaussian fitting. Finally, the radial velocities were corrected to the heliocentric reference frame.

4. Building the velocity catalog

In order to generate a large catalog of galaxy velocities to be used in the analysis below and in further studies to be presented in Papers III and IV, the 2868 velocity determinations presented above were combined with additional data previously published by us or obtained by other authors. In order to cover enough area, we searched the literature for velocities between $12^h 40^m < \alpha < 14^h 10^m$, and $-39^\circ < \delta < -23^\circ$. Table 2 lists the references, including an unpublished set kindly provided by D. Proust (private communication). Many galaxies have been observed more than once (both in different data sets or within our own observations), which allows us both to obtain more accurate velocity determinations for these galaxies and to compare different data sets for general quality of the data and possible zero-point shifts. Below, we describe how we combine the different data sets to build a coherent catalog.

4.1. Comparison

First, we compare the velocities of 241 galaxies observed by us more than once in different sessions. Figure 2 shows the residuals of the velocities measured with fibers as a function of the internal error for these galaxies. A zero-order polynomial fitting of the data with a 3σ clip gives a mean residual of $\sim 16 \text{ km s}^{-1}$ with an rms of $\sim 70 \text{ km s}^{-1}$, which is consistent with the average external errors of $\sim 70 \text{ km s}^{-1}$ for the Las Campanas Redshift Survey (Shectman et al. 1996). However, if we assume that the quoted errors for the galaxies are good estimates of the cross-correlation errors, we can compute the mean and the rms of $(v_{fib1} - v_{fib2})/\sqrt{\sigma_{fib1}^2 + \sigma_{fib2}^2}$ in order to estimate the true statistical errors of the data. We obtain a mean of -0.31 and rms of 1.57 . These results show that the velocity zero-point correction is negligible, and that the cross-correlation errors are, on average, 1.57 times smaller than the true errors. Similar correction factors were obtained by Malamuth et al. (1992) (1.6) and Bardelli et al. (1994) (1.87). As final velocity errors, we adopt the cross-correlation errors multiplied by 1.57, unless this result turns out to be less than 50 km s^{-1} . In this case, we take the latter constant value as the velocity uncertainty of the galaxy, as any smaller values are likely to be statistical artifacts.

In order to combine our data with those from the literature, we normalized all radial velocity sets to a common zero-point. If the zero-points of different instruments differed by significant amounts, we could introduce serious systematic errors in the resulting velocity dispersion and in the dynamical analysis. Table 2 summarizes the results of the zero-point shifts obtained from comparison of our data with the previously published ones, totaling 919 velocities, where, for each set, we present the number of galaxies in common with the present fiber observations. A large set of data came from our previous work (Paper I: codes Q5, Q7), using the same telescope, the LCO spectrograph with the same grating, and similar detectors. Therefore, one should expect small systematic differences between these

data sets. Figure 3 shows the residual for 65 galaxies in common with Paper I (data sets Q5 and Q7). The mean difference between both data sets (8 km s^{-1} , with an rms of 83 km s^{-1}) is negligible and well within individual errors. It is also consistent with fiber-to-fiber comparisons. This confirms the consistency between the fiber and Shectograph data, allowing both data sets to be treated as one. We have applied the zero-point shift given in Table 2 to all velocities of the literature before combining them into a final average value. For references without velocities in common with our data, or when the number of velocities was too low to obtain a meaningful shift (for example, Dressler & Shectman 1988), we compared the data with other data sets in the literature, calculating the zero-point shift in a transitive way.

4.2. Final Average Velocities

The average velocity for galaxies with multiple references was calculated following Quintana et al. (1996). This final velocity is a weighted mean velocity given by

$$\bar{V} = \frac{\sum_i w_i v_i}{\sum_i w_i} \quad (1)$$

where v_i is the galaxy velocity, $w_i = 1/\sigma_i^2$ is the weighting factor, and σ_i is the uncertainty. The weighting factor w_i came from our internal uncertainties or from the published uncertainties. Our internal uncertainties were obtained from the XCSAO cross-correlation program as $\sigma_{int} = 0.75W/(1+R)$, where R is the Tonry-Davis number and W is the FWHM of the parabola used to fit the correlation peak, corrected by 1.57 as discussed in §4.1.

Different criteria were used to calculate the error of the weighted mean velocity. These criteria depend upon whether we considered all velocities to be of comparable quality or not (beyond their formal errors):

1. If we assume that all velocities are fully believable, then we use

$$\sigma_{\mu err} = \frac{1}{\sqrt{\sum_i w_i}} \quad (2)$$

as the error of the weighted mean.

2. If we assumed the quoted velocity errors to be only weights and not to represent the true velocity errors, the uncertainty of the weighted mean is given by the weighted *rms* dispersion

$$\sigma_{\mu W} = \sqrt{\left(\frac{\sum_i w_i v_i^2}{\sum_i w_i} - \bar{V}^2\right) \times \frac{1}{N-1}} \quad (3)$$

3. If internal uncertainties adequately measure the external uncertainties, and if the number of the individual measurements is large, both ways should give the same results in the mean, but $\sigma_{\mu err}$ is too low if internal uncertainties underestimate external ones, and $\sigma_{\mu W}$ is too low if by chance the measured values are close to each other. To detect whether the differences between measured values are clearly larger than the internal uncertainties or not, we compared the unweighted *rms* dispersion $\sigma_{UW} = \sqrt{\sum_i (v_i - \bar{V})^2 / N(N-1)}$ to $\sigma_T = \sqrt{\sum_i \sigma_i / (N-1)}$, as a criterion to estimated the error of the weighted mean velocity. The criterion is the following: *i*) if $\sigma_{UW} > 2\sigma_T$, we don't have any information about which measurement is correct (systematic errors should be blamed), so the uncertainty of the weighted mean is given by σ_{UW} , without dividing by \sqrt{N} ; *ii*) if the anomalous case detected had values of $\sigma_{\mu W}$ and σ_T lower than 50 km s^{-1} , we assumed $\sigma_{\mu W}$ (eq. 3).

In a few cases we have discarded a velocity when analysis of the spectra, the galaxy morphology, or other details show discrepancies which are large compared to the

measurement error. Velocities reported in the literature which differed by $> 200 \text{ km s}^{-1}$ from our own determination for the same galaxy were discarded before combining.

The final sample resulting from this procedure contains 5090 galaxies with known redshifts. Of these, 2627 were observed by us, including 567 in common with the literature, and 2060 for which this is the first velocity determination. Therefore, the present study contributes 41% of the presently available sample of galaxies in the region (and an even higher fraction in the restricted region covered by this study and in the redshift range corresponding to the SSC).

5. Morphology

The full sample of galaxies to be used in the present study and in those following it (Papers III and IV) is presented in Figures 4 - 7. Their spatial distribution, shown in Figure 4, makes it clear that the area, particularly outside our original survey, is covered in a very sparse and patchy way. In addition, it has to be stressed that, even in the areas covered by the surveys, this sample does not have a well-defined completeness limit². This has to be kept in mind and should deter us from overinterpreting the apparent structures. On the other hand, the level of detail visible in all these figures makes it clear that a more detailed assessment of the complex morphology of this region, particularly of the SSC itself, should now be possible.

The histogram in Figure 5 presents four maxima. The main body of the SSC is represented by the highest peak, which is centered at $\sim 15,000 \text{ km s}^{-1}$ and extends over

²Based on the COSMOS/UKST galaxy catalog of the southern sky (Yentis et al. 1992), we estimate the completeness of our own data, in the regions covered, to be $\sim 75\%$ down to $b_j < 18.5 \text{ mag}$.

the velocity range 13,000 - 18,000 km s⁻¹. Another peak between 9,000 and 13,000 km s⁻¹ shows a foreground structure connected to the SSC. This can be seen better in the cone diagram of Figure 6 (right ascension projection). The other two peaks are at 4,000 km s⁻¹ (the Hydra-Centaurus connection and the “Great Attractor” region) and at 23,000 km s⁻¹ (another possible supercluster behind the SSC). Figures 5 and 7 also show a few “clumps” at higher redshift. The cone diagram confirms the presence of a large void in the velocity interval 18,000 - 22,000 km s⁻¹ behind the SSC (cf. Bardelli et al. 2000).

5.1. The Shapley Supercluster

The definition of the extension of the Shapley Supercluster is not an easy task, because of the complexity of the structures in the velocity distribution and the limited extension of the velocity survey on the plane of the sky. The presence of many clusters, with their characteristic finger-of-God velocity structures, complicates the study. Moreover, the remaining irregularities and gaps in the observations can mimic apparent structures. Finally, as today’s redshift surveys show, dense structures are linked by filaments and walls, forming a fabric that completely fills the space. Therefore, we can expect that the SSC will be linked to foreground and background structures, as well as others on the plane of the sky.

Where does the SSC proper end? Several criteria can be used as definitions for its extent, such as cluster or galaxy density or density contrast, percolation criteria, and others. Without a redshift survey over a wider area, we feel we cannot address this question more reliably than has been done before (e.g., Zucca et al. 1993; Einasto et al. 1997). As a preliminary criterion, based primarily on the velocity histogram of Figure 5, we will consider as SSC members all galaxies and clusters in the area surveyed that have a redshift $9,000 \leq v \leq 18,000$ km s⁻¹, corresponding to a total depth of $90h^{-1}$ Mpc. These limits are

supported by the cone diagrams, which also clearly show voids of much lower density, both in front and behind this structure. In this redshift range, there are 2949 redshifts in the total sample, allowing a fairly detailed study of the SSC’s structure.

Because of the limited sky coverage of the redshift surveys, the transverse dimensions of the SSC are less clear, but it appears to cover much of the surveyed area, or at least $35 \times 25h^{-2}$ Mpc². In this volume, quite elongated along the line of sight, the central region of the SSC, centered on the rich cluster A 3558, is quite outstanding. Several filaments and sheets of galaxies are also apparent, extending at different densities between the central region and surrounding groups of clusters, as detailed below. Galaxy clusters in this region include many ACO clusters, in addition to other groups and clusters that have been identified, particularly from X-ray surveys. Among these are the poor clusters SC 1327-312 and SC 1329-314 (Breen et al. 1994) and the ROSAT cluster RX 1252.5-3116 (Pierre et al. 1994), which have recently been found through x-ray and optical observations, and the groups SC 1336-314, SC 1340-294, and SC 1342-302 found in the present study (see Paper IV for more details). The full list of clusters in the surveyed region is given in Table 3, and their positions are shown on Figure 4.

Before entering into the detailed discussion of the supercluster’s morphology, we want to make an important point. In dense structures such as the SSC, the internal gravity can produce strong peculiar motions, which implies that relative redshifts are not an exact representation of relative distances, especially not on small scales. In particular, virialized clusters, roughly spherical in real space, produce the characteristic “finger-of-God” effect in redshift space, but also somewhat larger structures can be strongly affected. It is argued in Paper III that the central part of the SSC (within a radius $\sim 10h^{-1}$ Mpc of the main cluster, A 3558) is presently collapsing, with infall velocities ~ 1000 km s⁻¹. Therefore, objects within this region, with a somewhat *larger redshift* than A 3558, are probably *closer*

to us than A 3558 and falling towards it from the front side, while objects with somewhat *lower redshifts* are likely to be *further away*. The model described in Paper III is too crude to be expected to account for any details of the observed structures or to transform reliably from redshift space to real space, therefore the discussion below will be done *as if* redshift truly represented relative distance. This is a good approximation for redshift differences of several thousand km s^{-1} , but it should be kept in mind that it is unlikely to be correct for much smaller differences.

In the detailed study of the SSC’s substructures, we are guided by the wedge diagrams in Figure 6 and by many plots of the galaxy and cluster positions in velocity cuts of different depths, the most illuminating of which are presented in Figure 8. Although we obtain fairly clear identifications, we have to keep in mind the uncertainties introduced by the mentioned gaps and irregularities remaining in the velocity survey, so that our results are provisional and require confirmation when we complete the survey.

The *Central Region* of the SSC (CR), roughly spherical in shape, has at its core the highest-density, elongated region containing the Abell clusters A 3562, A 3558, and A 3556 (Fig. 8f), with almost identical recession velocities near 14400 km s^{-1} , and the groups SC 1329-314 (Fig. 8e) and SC 1327-312 (Fig. 8h), whose more discrepant velocities (by several hundred km s^{-1}) could be attributed to infall along the line of sight. To the south of the elongated feature, the CR also contains the cluster A 3560 (Fig. 8g). Note that the very thin velocity slice of Figure 8f (chosen to eliminate other structures) does not do justice to the extreme galaxy richness of this region. Given its high velocity dispersion, the CR can be seen over Figures 8d through 8i. The whole of this central region and all of its immediate surroundings are within the volume which, according to the study of Paper III, is currently undergoing gravitational collapse. Therefore, in this volume, *redshift should anticorrelate with distance*.

From this central region, a wide wall of galaxies, groups and clusters, which we hereafter call the *Front Eastern Wall* (FEW), extends to the east and front of the supercluster at $\sim 10,000 - 11,000 \text{ km s}^{-1}$ in redshift (Fig. 8c). The densest part of this wall is a filament running eastward at a declination just south of the CR and containing the newly identified group SC 1336-314 and the clusters A 3571/3572/3575. A 3570 is located at the southern tip of the observed part of the FEW, and A 3578 may mark its northern end, which is less well sampled. The northern part of the FEW has rather low galaxy density, but is wider (along the line of sight) than the southern part and connects to the cluster A 1736a and another, unidentified group just south-east of it (Fig. 8b). From these, a filament runs to the south-west, connecting to A 3537a (Fig. 8a).

Another major feature is the wide, dense *North-West Filament* (NWF) that from the CR runs first SW and then turns to the NW, going behind and away from the CR. It includes A 3554, A 726S, A 724S, and A 3544 in the SW (Figs. 8f-g), A 3537b further west (Fig. 8h), and finally the group of rich X-ray clusters A 3528/3530/3532, and RX J1252.5-3116, all in a narrow redshift range and prominently visible on Fig. 8i, at the furthest point of the SSC, both in redshift and in angular position. Also associated with this filament may be the clusters A 3552,³ A 3553, A 731S, A 729S, and A 718S (Figs. 8g-h), which do not follow the filamentary structure, but are spatially close to it and in the same redshift range. The specific initial direction and later turn of the NWF observed in the data may be an artifact of the gap in observed galaxies in this region, and are certainly

³The existence of A 3552 as a true cluster is doubtful: No X-rays have been detected from it, and at its position only a small group of galaxies can be found concentrated in redshift. Its previous, large mass measurements (e.g., Paper I) are likely an artifact of having included a number of “field” galaxies which, as they belonged to the SSC, showed a smoothly peaked, but very extended redshift distribution.

affected by the internal dynamics (peculiar velocities) in the SSC.

The last major feature of the SSC is the *Northern Extension*, a broad arm running N from the CR and to progressively lower redshift (Fig. 8e), connecting to the clusters A 3557a ($v \approx 14,300 \text{ km s}^{-1}$; Fig. 8f), A 3559 and A 3555 ($v \approx 14,000 \text{ km s}^{-1}$), A 1736b ($v \approx 13,600 \text{ km s}^{-1}$), and beyond.

There are two other minor arms or filaments extending out from the CR:

- a) Behind the FEW and at slightly higher redshift than the CR (Fig. 8g), a diffuse filament from the CR to the North-East leads through the new cluster SC 1342-302 to A 3577.
- b) From the CR to the SE and to higher redshift (Fig. 8h), a broad arm connects to the group of clusters A 3564, A 3566, A 3568, and A 742S (all with $v \approx 15,200 - 15,500 \text{ km s}^{-1}$). This arm shows a dense cloud just north of the catalog position of A 3568, which may be part of this cluster (if its catalog center position were somewhat off), or an artifact of the galaxy selection at the edges of the fiber plates.

5.2. Background structures

On the high-redshift side of the central concentration, a large, very low density void, also identified by Bardelli et al. (2000) as *V1*, opens up and extends from $\sim 18,000$ to $21,000 \text{ km s}^{-1}$ (see Figs. 5, 6, 7, and 8j). The only two clusters on Fig. 8j are near the upper end of this redshift range, and at the south and west edges of the studied area.

Behind the void, there appears a low-density, transverse, S-shaped filament at $v \approx 21,300 \text{ km s}^{-1}$, extending diagonally across the surveyed area (Fig. 8k). Possibly connected to it is the most prominent of all structures appearing behind the SSC. This structure

appears as a strong peak around $23,000 \text{ km s}^{-1}$ in the velocity histogram (Fig. 5), and can be seen in more detail in Figure 8l. It extends only $\sim 2000 \text{ km s}^{-1}$ in redshift and $\sim 25h^{-1} \text{ Mpc}$ in its larger transverse dimension, but contains six Abell clusters (in order of increasing redshift, A 3545/3524/3531/3549/1648/3557b), in addition to the new cluster, SC 1340-294, and another candidate cluster near 12^h55^m in right ascension and -29° in declination. In the better sampled area in the center of Figure 8l, it can be seen that the clusters are also connected by abundant intercluster galaxies. Thus, we believe that this concentration is most aptly described as another supercluster.

Beyond this redshift, the coverage of our sample is not much better than the one studied by Bardelli et al. (2000), which has been included. For this reason, we do not go into details of its analysis. Fig. 7 shows essentially the same structures (concentrations and voids) that have been identified by Bardelli and collaborators. The possible superclusters S300a and S300b are clearly present (both are at right ascension $\sim 13^h10^m$, at redshifts $\approx 32,000$ and $40,000 \text{ km s}^{-1}$, respectively), but not much structure can be seen within them, although hints of some clusters of galaxies are apparent in S300a, which will be further studied in Paper IV. We only add that both candidate superclusters seem to be connected by a bubble-like structure surrounding the void V3 and including on its surface the cluster A 3551 ($v \approx 37,500 \text{ km s}^{-1}$).

6. Conclusions

The large number of new redshift determinations in the Shapley Supercluster region brings the total number of available galaxy redshifts in the SSC to 2949. For comparison, the next best-sampled superclusters are Corona Borealis, for which this number is 528 (Small et al. 1997), and the Hercules Supercluster, with 468 available velocities (Barmby & Huchra 1998). This allows to analyze the morphology of this supercluster in much more

detail than is possible elsewhere. We show that several structures extend outward from the supercluster core, linking it to groups of galaxy clusters up to $\sim 40h^{-1}$ Mpc away. We also find a few new clusters or groups in the SSC region, and identify another supercluster in the background at $\sim 23,000$ km s $^{-1}$.

We are grateful to D. Proust for making his redshift data available to us prior to publication. We also thank the Director of the Observatories of the Carnegie Institution of Washington for generous allocation of telescopes at Las Campanas Observatory. This work benefitted from the use of the NASA/IPAC Extragalactic Database (NED), which is operated by the Jet Propulsion Laboratory, California Institute of Technology, under contract with the National Aeronautics and Space Administration. It was financially supported by FONDECYT grant 8970009 (*Proyecto de Líneas Complementarias*), and by a Presidential Chair in Science awarded to HQ. ERC was funded by FAPESP PhD fellowship 96/04246-7.

REFERENCES

- Abell, G. O., Corwin, H. G., & Olowin, R. P. 1989, *ApJS*, 70, 1: ACO
- Allen, D., Norris, R. P., Meadows, V. S., & Roche, P. F. 1991, *MNRAS*, 248, 528
- Bardelli, S., Zucca, E., Vettolani, G., Zamorani, G., Scaramella, R., Collins, C. A., & MacGillivray, H.T. 1994, *MNRAS*, 267, 665
- Bardelli, S., Zucca, E., Zamorani, G., Vettolani, G., & Scaramella, R. 1998, *MNRAS*, 296, 599
- Bardelli, S., Zucca, E., Zamorani, G., Moscardini, L., & Scaramella, R. 2000, *MNRAS*, 312, 540
- Barmby, P., & Huchra, J. P. 1998, *AJ*, 115, 6
- Batuski, D. J., Miller, C. J., Slinglend, K. A., Balkowski, C., Maurogordato, S., Cayatte, V., Felenbok, P., & Olowin, R. 1999, *ApJ*, 520, 491
- Breen, J., Raychaudhury, S., Forman, W., & Jones, C. 1994, *ApJ*, 424, 59
- Carrasco, E. R., Quintana, H., & Reisenegger, A. 2000, in preparation: Paper IV
- Cristiani, S., de Souza, R., D’Odorico, S., Lund, G., & Quintana, H. 1987, *A&A*, 179, 108
- da Costa, L. N., Nunes, M. A., Pellegrini, P. S., Willmer, C., Chincarini, G., & Cowan, J. J. 1986, *AJ*, 91, 6
- da Costa, L. N., Willmer, C., Pellegrini, P. S., & Chincarini, G. 1987, *AJ*, 93, 1338
- Dressler, A., & Shectman, S. 1988, *AJ*, 95, 284
- Dressler, A. 1991, *ApJS*, 75, 241

- Drinkwater, M. J., Proust, D., Parker, Q. A., Quintana, H., & Slezak, E. 1999, PASA, 16, 113
- Einasto, M., Tago, E., Jaaniste, J., Einasto, J., & Andernach, H. 1997, A&AS, 123, 119
- Ettori, S., Fabian, A. C., & White, D. A. 1997, MNRAS, 289, 787
- Hanami, H., Tsuru, T., Shimasaku, K., Yamauchi, S., Ikebe, Y., & Koyama, K. 1999, ApJ, 521, 90
- Jacoby, G. H., Hunter, D. A., & Christian, C. A. 1984, ApJS, 56, 257
- Kull, A., & Böhringer, H. 1999, A&A, 341, 23
- Kurtz, M. J., Mink, D. J., Wyatt, W. F., Fabricant, D. G., Torres, G., Kriss, G. A., & Tonry, J. L. 1992, in *Astronomical Data Analysis Software & Systems I*, D. M. Worrall, C. Biemesderfer, and J. Barnes, eds., ASP Conf. Ser. Vol. 25 (ASP, San Francisco), p. 132
- Malamuth, E. M., Kriss, G. A., Van Dyke Dixon, W., Ferguson, H. C., & Ritchie, C. 1992, AJ, 104, 495
- Melnick, J., & Quintana, H. 1981, A&AS, 44, 87
- Melnick, J., & Moles, M. 1987, RMxAA, 14, 72
- Metcalf, N., Godwin, J.G., & Spencer, S.D. 1987, MNRAS, 225, 581
- Pierre, M., Böhringer, H., Ebeling, H., Voges, W., Schuecker, P., Cruddace, R., & MacGillivray, H. 1994, A&A, 290, 725
- Pickles, A. J. 1985, ApJ, 296, 340
- Quintana, H., & de Souza, R. 1993, A&AS, 101, 475

Quintana, H., Ramírez, A., Melnick, J., Raychaudhury, S., & Slezak, E. 1995, *AJ*, 110, 463:

Paper I

Quintana, H., Ramírez, A., & Way, M. J. 1996, *AJ*, 112, 36

Quintana, H., Melnick, J., Proust, D., & Infante, L. 1997, *A&AS*, 125, 247

Raychaudhury, S. 1989, *Nature*, 342, 251

Raychaudhury, S. 1991, in *Clusters and Superclusters of Galaxies: Contributed Talks and Poster Papers*, M.M. Colless et al., eds. (IoA, Cambridge), p. 3

Raychaudhury, S., Fabian, A. C., Edge, A. C., Jones, C., & Forman, W. 1991, *MNRAS*, 248, 101

Reisenegger, A., Quintana, H., Carrasco, E. R., & Maze, J. 2000, *AJ*, in press: Paper III

Richter, O. G. 1987, *A&A*, 67, 261

Scaramella, R., Baiesi–Pillastrini, G., Chincarini, G., & Vettolani, G. 1989, *Nature*, 338, 562

Shapley, H. 1930, *Harvard Coll. Obs. Bull.*, 874, 9

Shectman, S. A. 1989, *Carnegie Institution of Washington Year Book* 89, p. 25-32

Shectman, S. A., Landy, S. D., Oemler, A. A., Tucker, D. L., Lin, H., Kirshner, R. P., & Schechter, P. L. 1996, *ApJ*, 470, 172

Small, T., Sargent, W., & Hamilton, D. 1997, *ApJS*, 111, 1

Stein, P. 1996, *A&AS*, 116, 203

Stein, P. 1997, *A&A*, 317, 670

- Stoche, J. T., Morris, S. L., Gioia, I. M., Maccacaro, T., Schild, R., Wolter, A., Fleming, T. A. & Henry, J. P. 1991, *ApJS*, 76, 813
- Teague, P.F., Carter, D., & Gray, P.M. 1990, *ApJS*, 72, 715
- Tonry, J., & Davis, M. 1979, *AJ*, 84, 1511
- Vettolani, G., Chincarini, G., Scaramella, R., & Zamorani, G. 1990, *AJ*, 99, 1709
- Vikhlinin, A., McNamara, B. R., Forman, W. & Jones, C. 1998, *ApJ*, 502, 558
- Yentis, D. J., Cruddace, R. G., Gursky, H., Stuart, B. V., Wallin, J. F., MacGillivray, H. T. & Collins, C.A. 1992, in *Digitised Optical Sky Surveys*, H. T. MacGillivray and E. B. Thomson, eds. (Kluwer, Dordrecht), p. 67
- Zucca, E., Zamorani, G., Scaramella, R., & Vettolani, G. 1993, *ApJ*, 407, 470

Fig. 1.— Two-dimensional distribution of the 2627 galaxies observed with the fiber spectrograph. The solid squares indicate the 34 observed fields. Each field covers $1.5^\circ \times 1.5^\circ$.

Fig. 2.— Residual of the heliocentric velocities as a function of the internal quadratic error for the 241 galaxies observed with the fiber spectrograph in different sessions. The solid line represents the zeroth-order polynomial fit. The average shift after 3σ clipping is -13 km s^{-1} , with a rms of 65 km s^{-1} . The cross-correlation errors are, on average, 1.57 times smaller than the true statistical errors.

Fig. 3.— Residual of the heliocentric velocity as a function of the internal quadratic error for the 65 galaxies in common with our previously published data (Q5, Q7 in Paper I). The mean shift of 8 km s^{-1} is negligible compared to the 83 km s^{-1} rms of the residuals, and consistent with the fiber-to-fiber comparison.

Fig. 4.— Both panels show the two-dimensional distribution of the full sample of galaxies studied in the present paper, including new data and data from the literature between $12^h 40^m < \alpha < 14^h 10^m$, and $-39^\circ < \delta < -23^\circ$. The open circles represent the positions of the clusters of galaxies given in Table 3. Panel (a) shows the clusters with known redshifts in the range of the SSC, $9,000 < v < 18,000 \text{ km s}^{-1}$, with the sizes of the circles representing the Abell radius, $1.5h^{-1} \text{ Mpc}$, at the distance inferred from their individual redshifts. Panel (b) shows all other clusters, i.e., all those whose redshifts are either unknown or outside the SSC range. In this case, the size of the circles was taken inversely proportional to their ACO distance class. Clusters without a distance class are shown as crossed circles.

Fig. 5.— Radial velocity distribution for galaxies observed by us (dashed histogram) and for the total sample including data from the literature (open histogram), with $v < 50,000 \text{ km s}^{-1}$.

Fig. 6.— Cone diagrams of all galaxies with known redshifts in the region limited by $12^h 50^m < \alpha < 14^h 05^m$, $-38^\circ < \delta < -24^\circ$, and $6,000 < v < 20,000 \text{ km s}^{-1}$. Panel (a) shows right ascension vs. radial velocity; panel (b) shows declination vs. radial velocity.

Fig. 7.— Cone diagrams of all galaxies with known redshifts in the region limited by $12^h 50^m < \alpha < 14^h 05^m$, $-38^\circ < \delta < -24^\circ$, and $18,000 < v < 50,000 \text{ km s}^{-1}$. Panel (a) shows right ascension vs. radial velocity; panel (b) shows declination vs. radial velocity.

Fig. 8.— Distribution on the sky of galaxies and clusters with known redshifts in thin velocity slices of various widths, illustrating the three-dimensional structure of the SSC and a background supercluster: (a) $9,000 < v < 10,000 \text{ km s}^{-1}$; (b) $10,000 < v < 11,000 \text{ km s}^{-1}$; (c) $11,000 < v < 12,000 \text{ km s}^{-1}$ (*Front Eastern Wall*); (d) $12,000 < v < 13,000 \text{ km s}^{-1}$; (e) $13,000 < v < 14,100 \text{ km s}^{-1}$ (*Northern Extension*); (f) $14,100 < v < 14,500 \text{ km s}^{-1}$ (*Central Region*); (g) $14,500 < v < 15,000 \text{ km s}^{-1}$; (h) $15,000 < v < 16,000 \text{ km s}^{-1}$; (i) $16,000 < v < 18,000 \text{ km s}^{-1}$ (end of *NW Filament*); (j) $18,000 < v < 21,000 \text{ km s}^{-1}$ (void *V1*); (k) $21,000 < v < 22,000 \text{ km s}^{-1}$; (l) $22,000 < v < 24,000 \text{ km s}^{-1}$ (background supercluster).

Table 1. Observing sessions

Session	SRC/ESO plate	Field id.	α_{2000}	δ_{2000}	t_{exp}	Code
			<i>h m s</i>	<i>° ' "</i>	s	
01/1992	444	444-A	13 23 50.6	-29 32 44	5400	QC01
	442/443 ^a	443-A	12 56 03.1	-29 32 01	5400	
05/1993	444 ^{a,b}	444-B	13 31 09.0	-30 44 25	5400	QC02
	444 ^{a,c}	444-C	13 31 09.0	-30 44 25	5900	
	444	444-D	13 24 11.7	-30 47 48	9000	
	383/444 ^{a,b}	383-A	13 31 27.5	-32 13 50	5400	
	383/444 ^{a,c}	383-B	13 31 27.5	-32 13 50	9000	
	382/383/444 ^a	383-C	13 24 19.4	-32 14 32	5400	
03/1994	382/443/444 ^a	382-A	13 18 50.1	-32 01 46	6000	QC03
	383/444/445 ^a	383-D	13 37 02.5	-32 06 14	6600	
	443/444 ^a	443-B	13 18 35.7	-30 46 49	7200	
	444/445 ^a	444-E	13 36 06.4	-30 52 53	6600	
	443/444 ^a	443-C	13 18 37.9	-29 30 54	7200	
	444	444-F	13 24 49.3	-29 31 41	7200	
	444	444-G	13 30 03.8	-29 30 33	10800	
	444/445 ^a	444-H	13 36 55.9	-29 33 04	8400	
05/1994	382	382-B	13 10 41.1	-33 15 30	3600	QC04
	382	382-C	13 17 18.0	-33 15 19	5400	
	382	382-D	13 23 51.8	-33 14 56	5400	
	383	383-E	13 30 24.5	-33 19 52	5400	
	383	383-F	13 36 27.7	-33 16 47	3600	
	443	443-D	13 12 39.3	-29 32 44	8100	
02/1995	443	443-E	12 56 52.7	-28 21 03	6600	QC05
	443	443-F	12 56 51.7	-30 44 21	7000	

Table 1—Continued

Session	SRC/ESO plate	Field id.	α_{2000} <i>h m s</i>	δ_{2000} <i>° ' "</i>	t_{exp} s	Code
	443	443-G	13 03 22.4	-30 46 02	5000	
03/1995	383	383-G	13 29 52.2	-34 45 27	4800	QC06
	383	383-H	13 42 51.6	-34 46 46	5100	
	443	443-H	13 03 04.7	-29 16 57	5400	
	443	443-I	13 05 31.7	-32 05 48	5400	
	444	444-I	13 24 48.5	-28 27 37	4800	
	444	444-J	13 30 54.2	-28 25 44	4800	
01/1996	445	445-A	13 43 07.3	-32 00 15	6600	QC07
	445	445-B	13 42 43.1	-30 25 14	7200	
	445	445-C	13 42 57.1	-28 57 04	7200	

^aOverlapping regions in SRC/ESO plates.

^bBright galaxies.

^cFaint galaxies.

Note. — Columns: 1. Date of observation. 2. ESO/SRC plate number. 3. Our internal field identification. 4. Right ascension of the field center. 5. Declination of the field center. 6. Exposure time. 7. Code for observing session.

Table 2. Zero point shift between fibers and the data from the literature.

References	N_{ref}	N_{comm}	ΔV km/s	$\sigma_{\Delta V}$ km/s	rms km/s
Bardelli et al. 1994	311	94	-5	10	93
Bardelli et al. 1998	174	73	-7	12	108
Bardelli et al. 2000	442	90	-7	16	102
Cristiani et al. 1987	44	35	50	26	90
Da Costa et al. 1986	111	29	-35	16	84
Da Costa et al. 1987	139	20	-38	19	82
Dressler 1991	545	22	-39	19	84
Drinkwater et. al. 1999	306	87	-9	12	110
Melnick & Quintana 1981	26	19	-65	73	93
Metcalf et al. 1987	40	27	10	15	70
Proust 2000 (private communication)	339	31	7	13	64
Quintana et al. 1995 (Q5 and Q7)	161	65	8	10	83
Quintana et al. 1995 (Q1 and Q2)	32	15	67	30	107
Quintana et al. 1995 (Q3,Q4,Q6,M1,M2,M3)	178	87	9	14	117
Quintana et al. 1997	298	43	27	14	74
Richter 1987	49	28	-43	20	94
Stein 1996	335	112	-17	5	46
Teague et al. 1990	90	25	69	17	77
Vettolani et al. 1990	42	17	4	19	68

Note. — Columns: 1. Reference. 2. Total number of galaxy redshifts. 3. Number of galaxies in common with the present work. 4. Mean velocity difference (zero-point shift) with respect to our work for galaxies in common. 5. Error in the zero-point

Table 3. Clusters of galaxies in the region $12^h 40^m < \alpha < 14^h 10^m$, $-39^\circ < \delta < -23^\circ$.

Name	α_{2000} <i>h m s</i>	δ_{2000} <i>° ' "</i>	BM	D	V [km/s]	Reference for V
A 3524	12 40 05.3	-34 13 28	I	5	22275	5
A 706S	12 41 05.3	-33 22 27	II-III	6		
A 1604	12 43 57.0	-23 06 25		6		
A 708S	12 44 23.9	-33 25 25	I	6		
A 3527	12 49 53.6	-36 45 00	I	6		
A 714S	12 51 28.9	-26 27 18	I	1		
VMF 98-124	12 52 05.4	-29 20 46			50965	8
VMF 98-125	12 52 11.3	-29 14 59				
RX J1252.5-3116	12 52 30.0	-31 16 00			16039	3
A 715S	12 53 06.2	-27 41 01	I	5		
A 1633	12 53 59.8	-26 23 00		6		
A 3528	12 54 22.2	-29 00 46	II	4	16365	2
A 3530	12 55 36.0	-30 20 51	I-II	4	16253	2
A 3531	12 57 05.4	-32 54 59	II	5	22454	1
A 3532	12 57 21.9	-30 21 47	II-III	4	16569	2
A 3535	12 57 54.7	-28 28 46	III	5	19986	2
A 717S	12 58 05.9	-28 12 59	I	5		
A 1648	12 58 59.6	-26 37 00		5	22994	1
A 718S	12 59 42.2	-33 39 59	I	4	14330	5
A 3537a	13 01 00.6	-32 26 00	I-II	2	9507	2
A 3537b	13 01 00.6	-32 26 00	I-II	2	15753	2
A 3540	13 03 18.1	-33 15 59	II-III	6		
A 1664	13 03 41.5	-24 12 59		6	38254	1
A 3541	13 03 41.5	-24 14 59	II-III	6	50665	1

Table 3—Continued

Name	α_{2000} <i>h m s</i>	δ_{2000} <i>° ' "</i>	BM	<i>D</i>	<i>V</i> [km/s]	Reference for <i>V</i>
A 721S	13 06 05.8	-37 34 59	II	4	14867	2
A 3542a	13 08 42.6	-34 32 59	I	4	27551	5
A 3542b	13 08 42.6	-34 32 59	I	4	39393	5
A 3543	13 09 23.9	-23 29 59	III	6		
A 3544	13 11 05.6	-32 59 00	I-II	6	14996	2
A 3545	13 11 23.5	-34 04 00	I-II	6	22245	5
A 3546	13 13 06.6	-29 58 00	I	6		
A 3547	13 13 17.6	-37 19 00	II?	6		
A 724S	13 13 17.6	-32 56 01	II	6	14775	2
A 725S	13 14 12.6	-30 11 00	II	6		
A 3549	13 14 23.6	-29 26 00	I-II	5	22634	5
A 726S	13 15 11.8	-33 38 51	II	5	14606	2
A 3551	13 18 11.9	-30 55 00	I-II	6	37522	2
A 3552	13 18 55.2	-31 49 03	I	6	15598	2
A 3553	13 19 14.6	-37 10 45	I-II	4	15110	4
A 3554	13 19 32.4	-33 29 15	I-II	4	14494	2
A 3555	13 20 20.8	-28 53 38	II	4	13950	2
A 728S	13 20 54.2	-27 17 59	II-III	5		
A 729S	13 21 29.9	-35 47 00	I	5	14960	4
A 730S	13 22 00.2	-26 58 00	I-II	5		
A 731S	13 22 59.3	-34 52 00	I-II	4	15140	5
A 3556	13 24 06.6	-31 40 12	I	4	14373	2
A 1727	13 24 12.2	-23 02 00		6		
A 732S	13 24 42.4	-26 01 00	II	6		

Table 3—Continued

Name	α_{2000} <i>h m s</i>	δ_{2000} <i>° ' "</i>	BM	D	V [km/s]	Reference for V
CL 1322-30	13 24 47.6	-30 17 37			4222	6
A 3557a	13 24 55.2	-28 53 16	I-II	5	14270	5
A 3557b	13 26 11.5	-28 47 34	I-II	5	23084	5
J132543.5-2944	13 25 43.5	-29 44 34				
A 733S	13 25 53.9	-37 13 59	II	5	20906	1
A 1736a	13 26 44.3	-27 26 22	III	2	10443	2
A 1736b	13 26 48.7	-27 08 38	III	2	13577	2
A 3558	13 27 56.9	-31 29 44	I	3	14390	2
SC 1327-312	13 29 47.0	-31 36 29	I-II		15124	2
A 3559	13 29 51.0	-29 30 51	I	4	13995	2
A 736S	13 31 00.6	-28 01 59	I-II	6		
SC 1329-314	13 31 36.0	-31 48 46	I-II		13388	2
A 3560	13 32 25.3	-33 08 12	I	3	14541	2
A 1757	13 33 32.9	-23 16 22		5	37894	1
A 3562	13 33 56.8	-31 29 23	I	3	14377	2
A 3564	13 34 24.0	-35 13 00	II	3	15188	2
SC 1336-314	13 36 19.0	-31 48 00			11857	2
A 3565	13 36 29.8	-33 58 17	I	1	3268	1
MS 1335.2-2928	13 38 05.8	-29 43 55			56661	7
A 3566	13 39 00.5	-35 32 59	II	4	15423	2
SC 1340-294	13 40 00.0	-29 46 00			23229	2
A 3567	13 39 48.6	-36 26 59	I-II	6		
A 3568	13 41 12.5	-34 38 00	II-III	6	15483	2
A 1771	13 42 11.6	-26 16 00		5	32048	1

Table 3—Continued

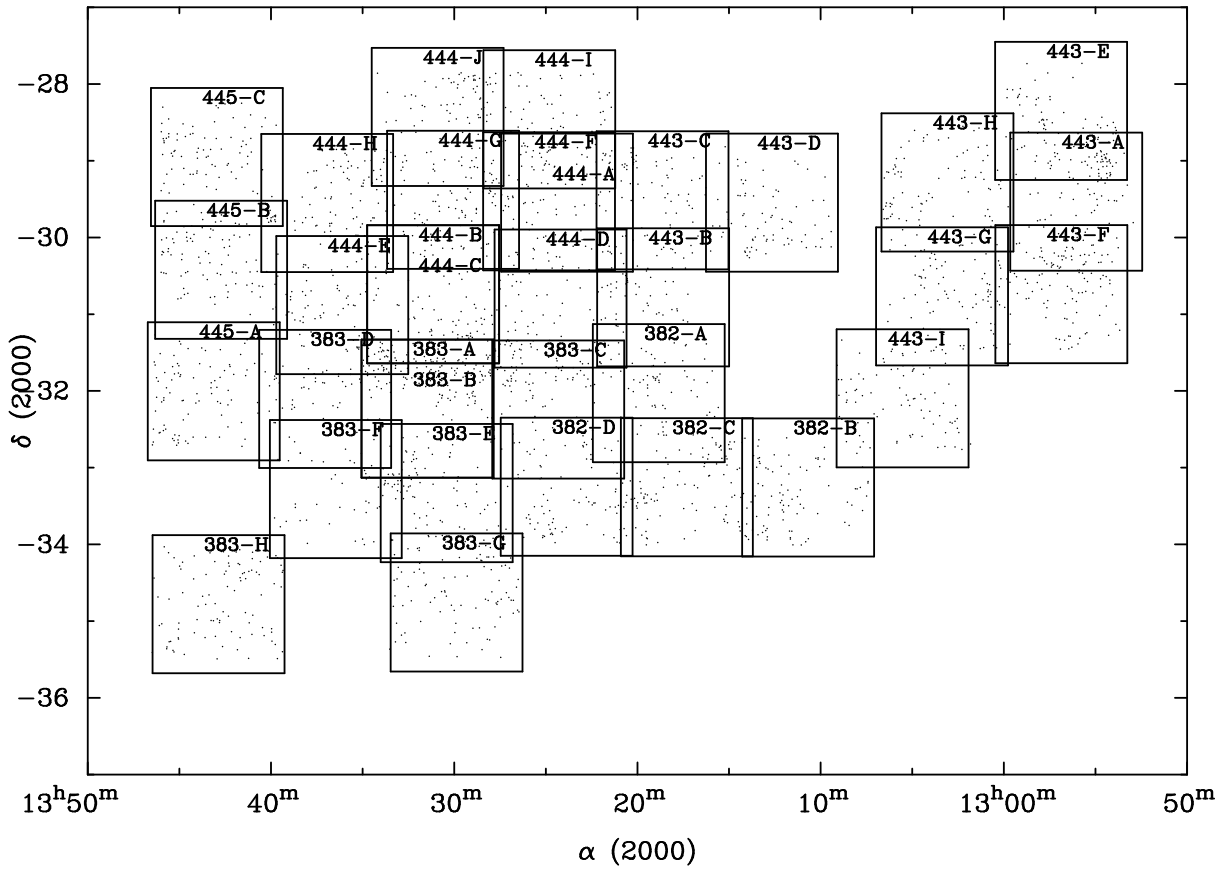
Name	α_{2000} <i>h m s</i>	δ_{2000} <i>° ' "</i>	BM	D	V [km/s]	Reference for V
A 3569	13 42 41.9	-35 45 01	I-II	6		
SC 1342-302	13 42 45.0	-30 20 00			14515	2
A 739S	13 42 54.3	-34 57 59	II	5		
A 740S	13 43 30.0	-38 10 59	I-II	3	10073	1
A 742S	13 44 36.0	-34 18 00	I-II	4	15277	2
A 3570	13 46 50.7	-37 54 58	I-II	4	11152	1
A 3571	13 47 28.3	-32 51 52	I	4	11730	4
A 744S	13 47 29.3	-32 07 59	I	5		
A 3572	13 48 11.9	-33 22 00	I-II	4	12141	1
A 745S	13 48 11.9	-36 27 59	III	6		
A 3573	13 48 24.3	-34 40 00	I	6		
A 1791	13 48 54.5	-25 26 00		5		
A 3574	13 49 05.4	-30 17 47	I	1	4227	1
A 746S	13 49 48.2	-34 57 59	II	4		
A 1794	13 50 11.5	-26 18 59		5		
A 747S	13 50 59.7	-36 06 59	II	5		
A 1802	13 51 24.4	-26 41 59		5		
A 3575	13 52 35.9	-32 51 59	II	4	11242	5
A 748S	13 52 35.9	-32 23 00	II	6		
A 3576	13 52 48.3	-30 16 59	I	6	44669	1
A 749S	13 52 59.3	-34 20 59	II:	6		
A 750S	13 53 36.4	-38 19 59	I-II	6		
A 751S	13 54 05.3	-25 42 59	I-II	6		
A 3577	13 54 17.7	-27 49 59	II	4	14870	5

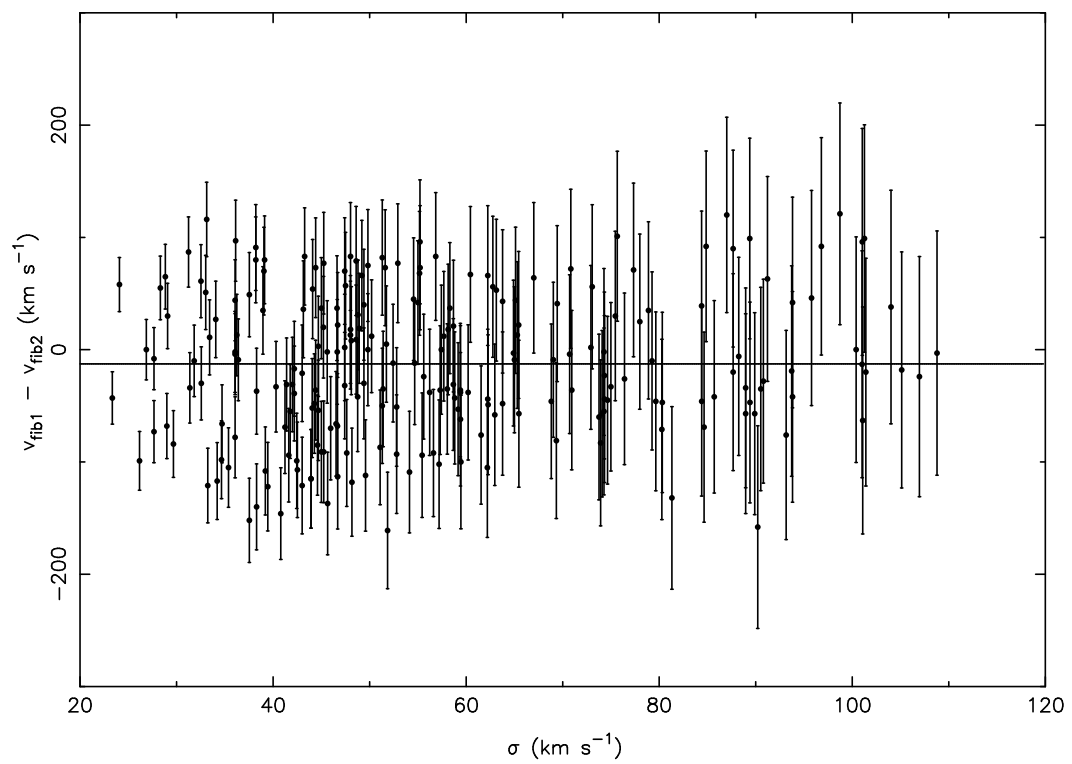
Table 3—Continued

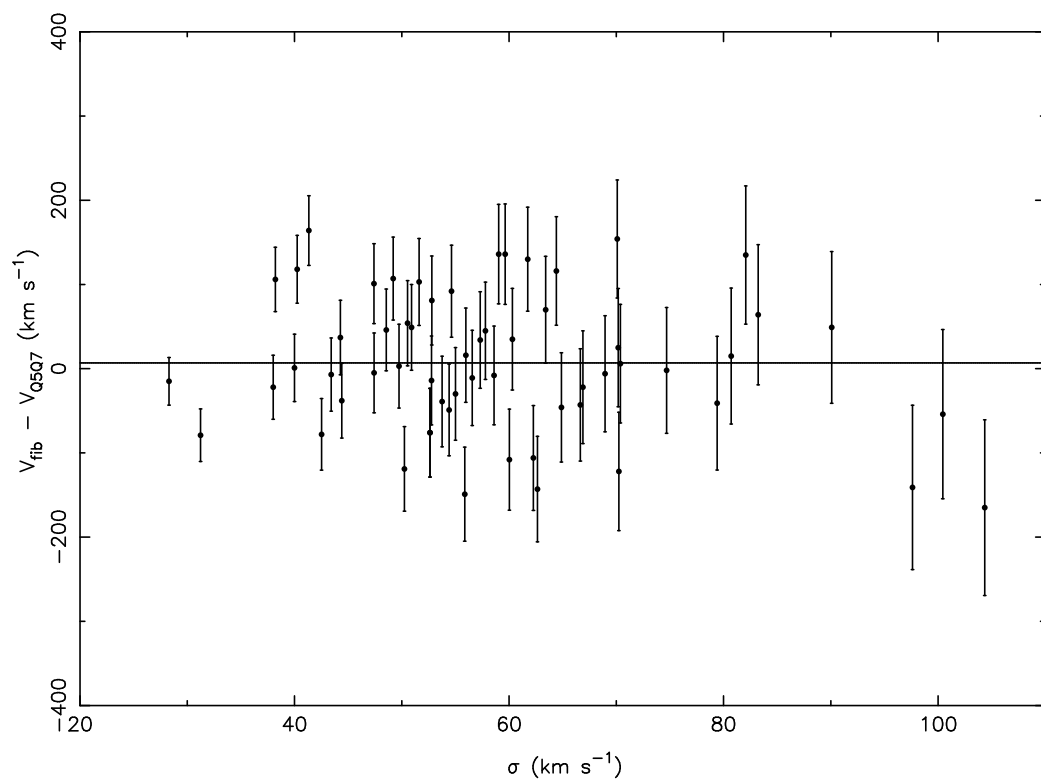
Name	α_{2000}	δ_{2000}	BM	D	V	Reference
	<i>h m s</i>	<i>° ' "</i>			[km/s]	for V
A 1816	13 55 41.6	-26 20 59		6		
A 3578	13 57 30.2	-24 43 00	I-II	3	11152	5
A 1822	13 58 29.3	-25 21 59		6		
A 3580	14 02 54.5	-23 43 25	I	6		
A 753S	14 03 38.5	-33 58 23	I	1	4197	1
A 1846	14 03 41.5	-25 21 59		6		
A 3581	14 07 29.7	-27 01 00	I	3	6416	1
A 1857	14 08 25.9	-27 01 15		6		

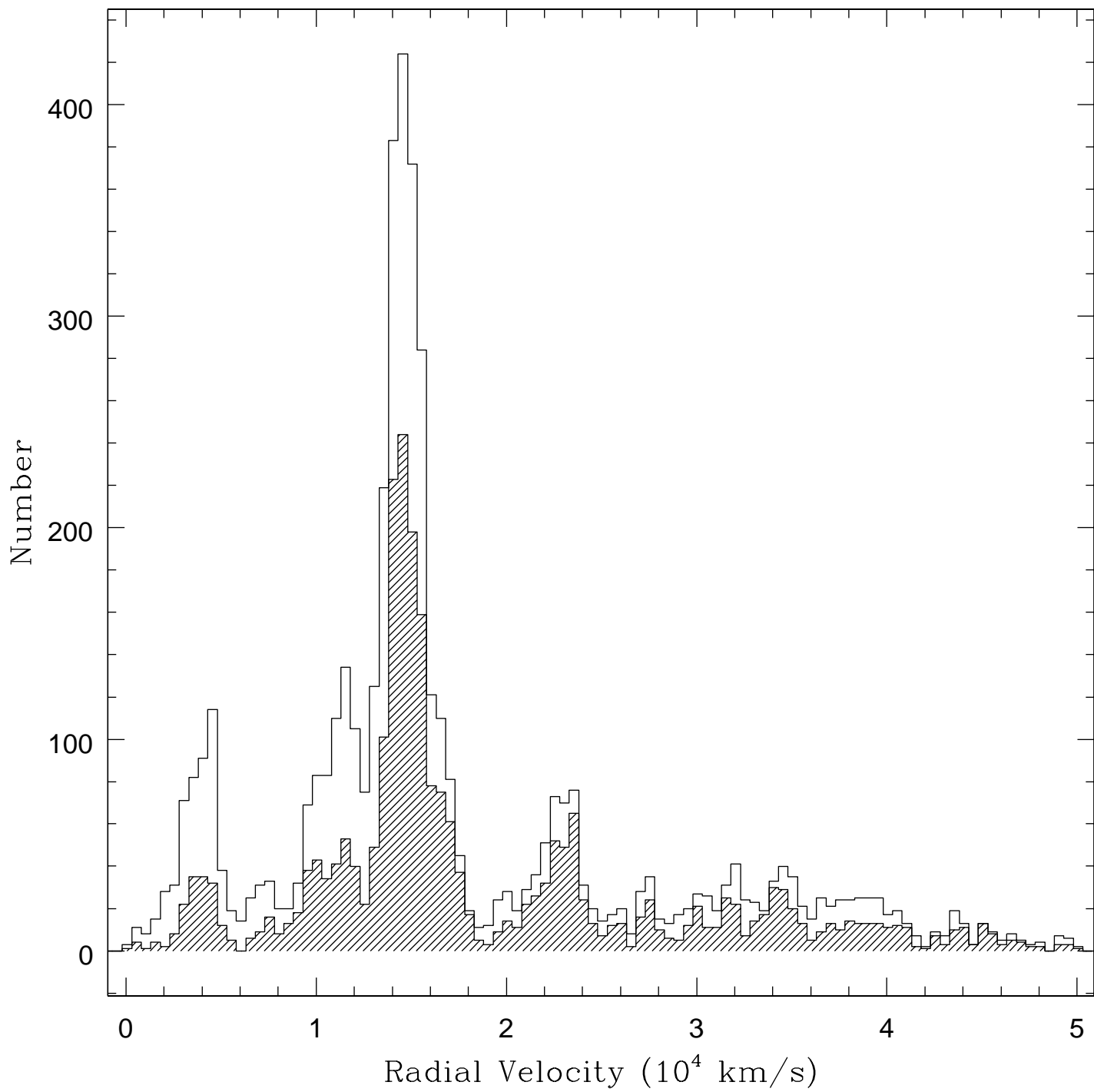
Note. — Columns: 1. Cluster identification. 2. Right ascension. 3. Declination. 4. Bautz-Morgan type. 5. Abell distance class (ACO). 6. Recession velocity (redshift). 7. Reference for the redshift.

References. — 1. Taken from the NASA/IPAC Extragalactic Database (NED); 2. Carrasco et al. (2000: Paper IV); 3. Pierre et al. (1994); 4. Quintana et al. (1995: Paper I); 5. Quintana et al. (1997); 6. Stein (1997); 7. Stocke et al. (1991); 8. Vikhlinin et al. (1998).

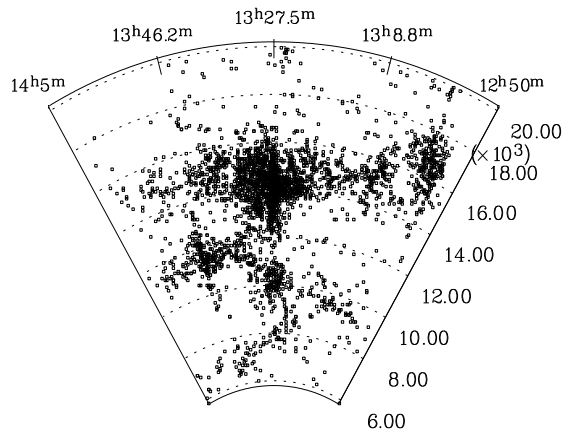




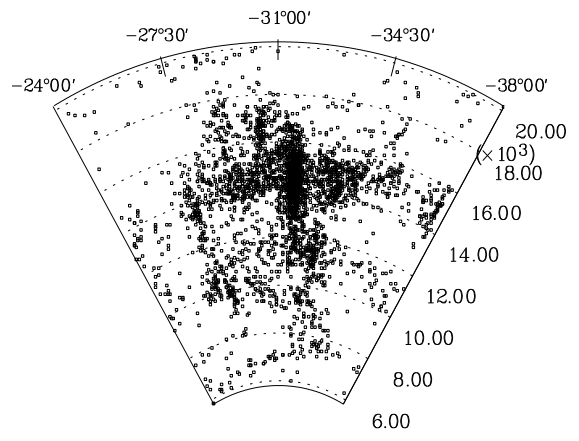




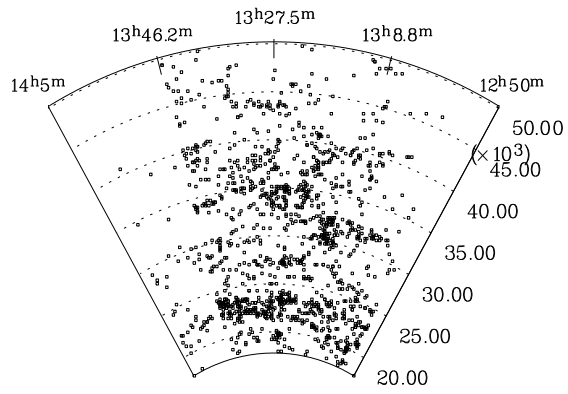
Right Ascension



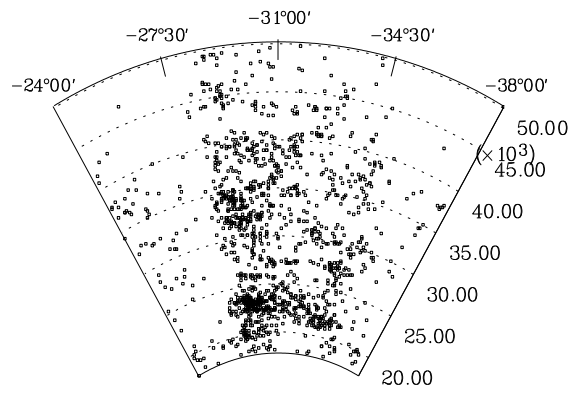
Declination



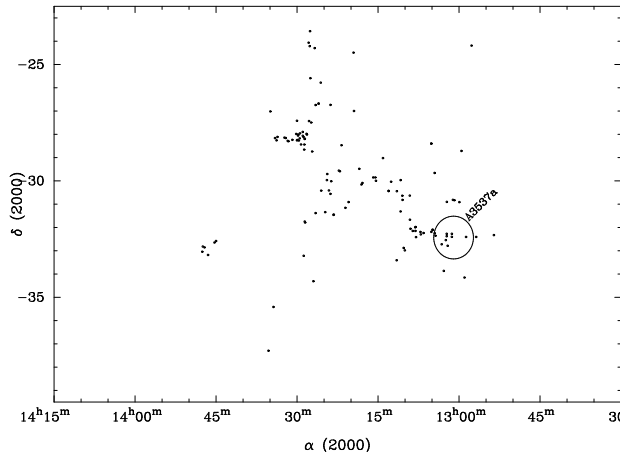
Right Ascension



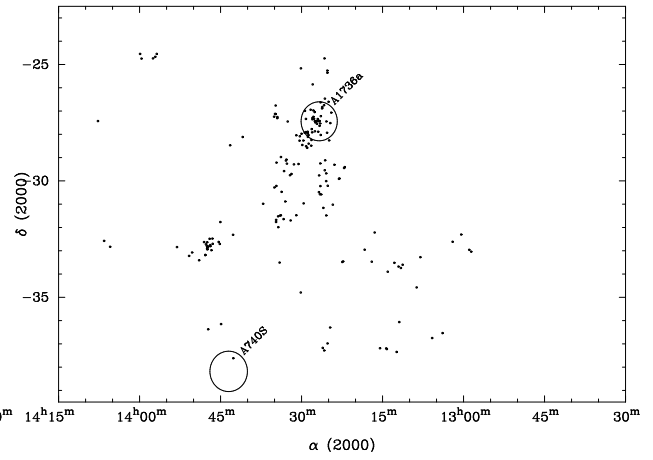
Declination



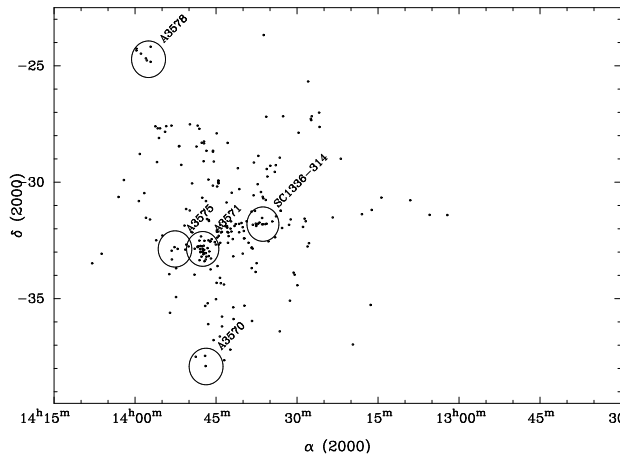
(a) $9000 \text{ km/s} < v < 10000 \text{ km/s}$



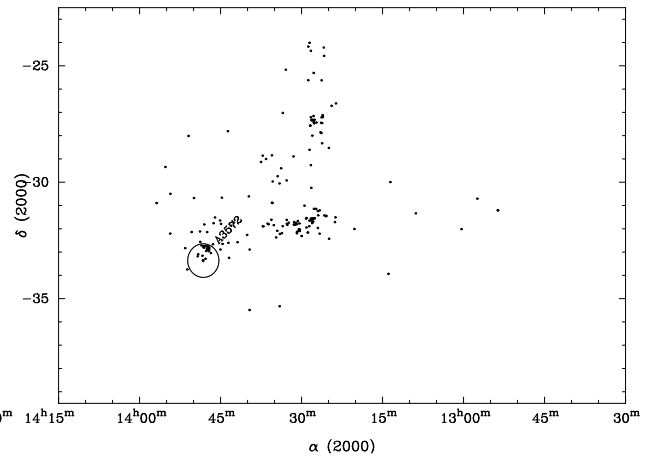
(b) $10000 \text{ km/s} < v < 11000 \text{ km/s}$



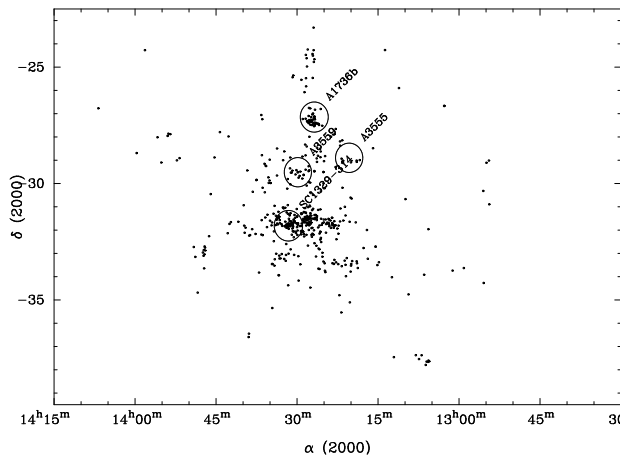
(c) $11000 \text{ km/s} < v < 12000 \text{ km/s}$



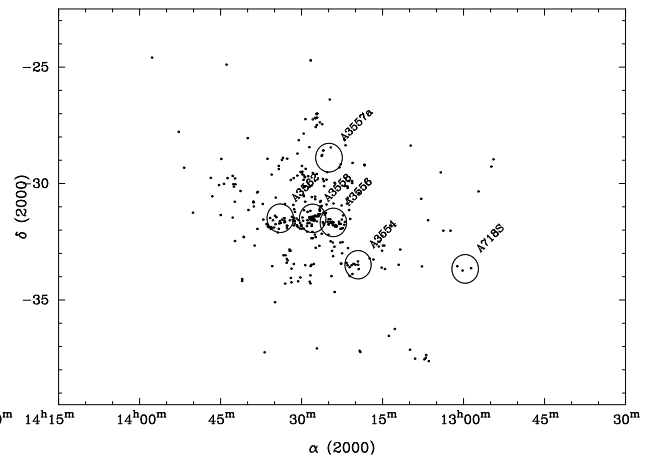
(d) $12000 \text{ km/s} < v < 13000 \text{ km/s}$



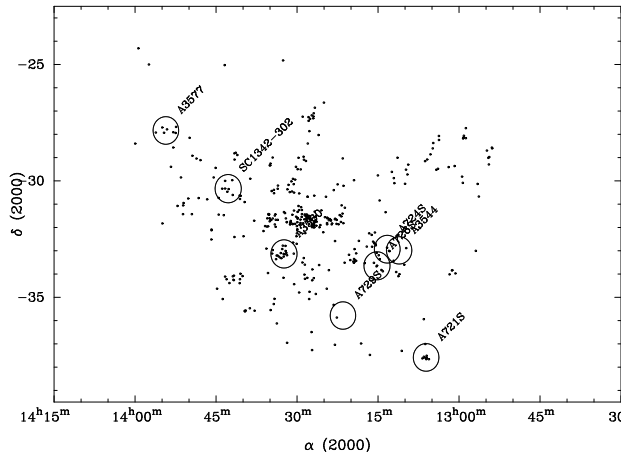
(e) $13000 \text{ km/s} < v < 14100 \text{ km/s}$



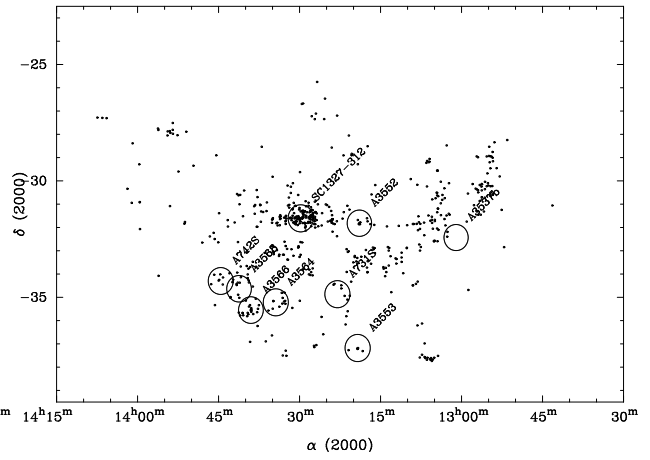
(f) $14100 \text{ km/s} < v < 14500 \text{ km/s}$



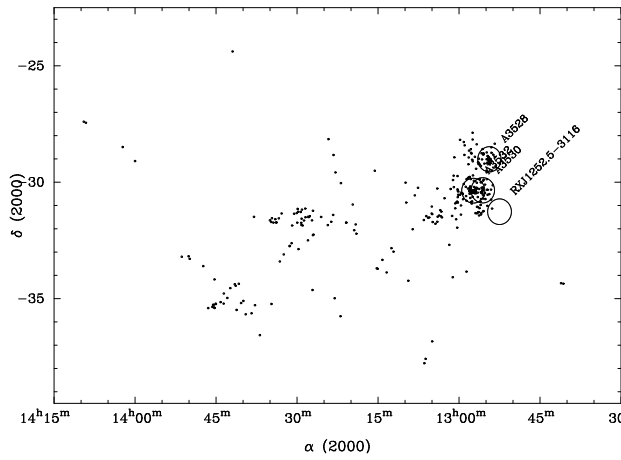
(g) $14500 \text{ km/s} < v < 15000 \text{ km/s}$



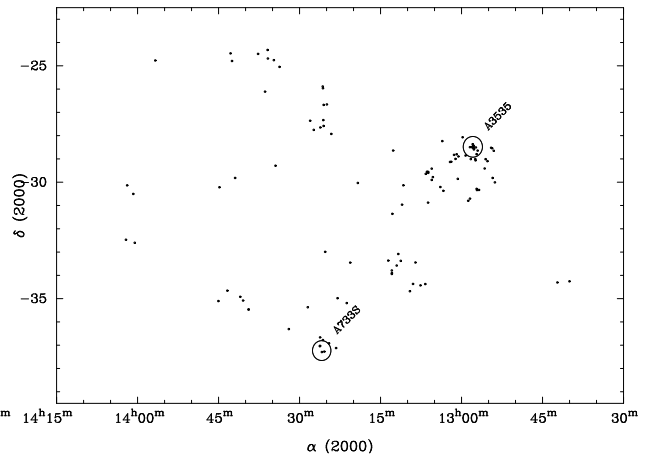
(h) $15000 \text{ km/s} < v < 16000 \text{ km/s}$



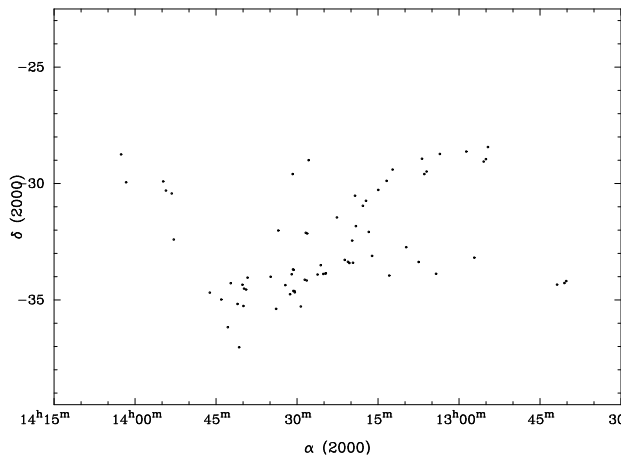
(i) $16000 \text{ km/s} < v < 18000 \text{ km/s}$



(j) $18000 \text{ km/s} < v < 21000 \text{ km/s}$



(k) $21000 \text{ km/s} < v < 22000 \text{ km/s}$



(l) $22000 \text{ km/s} < v < 24000 \text{ km/s}$

